



Symmetry-assisted anomalous Hall conductivity in a CrS₂-CrBr₃ heterostructure

Subhendu Mishra, Nikhilesh Maity, and Abhishek Kumar Singh ^{*}
Materials Research Centre, Indian Institute of Science, Bangalore 560012, India

 (Received 7 March 2024; revised 12 June 2024; accepted 15 August 2024; published 5 September 2024)

The symmetry-assisted anomalous valley Hall effect offers exciting prospects in valleytronics and spintronics. Here, using density functional theory and symmetry analysis, we propose an underlying mechanism for the fundamental origin of enhanced anomalous Hall conductivity σ_{xy} in the CrS₂ layer in the CrS₂/CrBr₃ heterostructure. Notably, we find that the magnetic proximity effect (MPE) induces an identical nature of spin magnetic moments from the magnetic CrBr₃ to nonmagnetic CrS₂ layer. For out-of-plane spin components ($0^\circ \leq \theta < 90^\circ$), in addition to orbital magnetic moments, induced magnetization and correction from Berry curvatures [$\Omega_z(\mathbf{k})$] leads to an additional contribution to σ_{xy} in the CrS₂ layer. Under in-plane magnetization directions, both time-reversal symmetry (\mathcal{T}) and out-of-plane mirror symmetry (\mathcal{M}_z) are broken; however, their joint operation is preserved. This joint symmetry operation guarantees Kramers spin degeneracy at the K and K' valleys, resulting in vanishing σ_{xy} . The exchange coupling between spins at valleys and magnetization directions induces an angular profile of σ_{xy} identical to the magnetic moment nature in the CrBr₃ layer. Our study reveals a potential approach to predict the variation of σ_{xy} in valley-polarized heterostructures through symmetry-assisted MPE and sheds light on understanding recent experimental findings in valleytronics.

DOI: [10.1103/PhysRevB.110.125406](https://doi.org/10.1103/PhysRevB.110.125406)

I. INTRODUCTION

The valley degree of freedom is rapidly emerging as a good quantum number analogous to charge and spin and has witnessed a growing interest in developing high-performance valleytronic devices [1–4]. Symmetry engineering is one of the most effective ways to control valley-driven properties in low-dimensional materials. Especially in two-dimensional (2D) transition-metal dichalcogenides (TMDCs), inversion symmetry (\mathcal{I}) breaking and strong spin-orbit coupling (SOC) result in two inequivalent valleys at K and K' in the Brillouin zone (BZ) [5]. This inversion asymmetry leads to a nonzero Berry curvature, allowing bulk valley transport via the valley Hall effect (VHE) [6]. Simultaneous breaking of time-reversal symmetry (\mathcal{T}) and \mathcal{I} while preserving their combined operation offers more promising transport phenomena, particularly the quantum anomalous valley Hall effect [7–10]. These valley-contrasting quantum effects provide a unique platform for exploring valley-based spintronics [11,12].

The key issue to realize such novel quantum phenomena is to break \mathcal{T} in valleytronic materials. Experimentally, valley polarization has been achieved in TMDCs by lifting valley degeneracy by an external magnetic field. However, the valley exchange splitting is observed to be very small, ~ 0.1 – 0.2 meV/T [13–15]. Recently, the magnetic proximity effect (MPE) has been revealed as a feasible and efficient approach to induce a large valley splitting in monolayer TMDCs [16–19]. Particularly, proximity-induced enhanced valley splitting has been experimentally observed in the WSe₂ monolayer placed on ferromagnetic (FM) EuS substrate [20],

whereas a giant valley polarization is theoretically found in Janus Pt dichalcogenide bound to magnetic EuO substrate [21]. Furthermore, the degree of valley polarization and splitting energy in TMDC monolayers is substantially modulated by the spin orientation of the magnetic layer [22,23]. A valley splitting of ~ 200 meV is achieved in a Mn/WS₂ van der Waals (vdW) heterostructure by rotating magnetic field direction [24]. Moreover, Zeeman fields arising from proximity-induced exchange coupling between spins at valleys and magnetization directions leads to a manipulation of anomalous Hall conductivity (AHC) in the 2H TMDC layer [25]. An enhanced spin-orientation dependent anomalous Hall effect (AHE) is also observed experimentally in the NbSe₂/V₅Se₈ heterostructure [26] and frustrated magnet KV₃Sb₅ [27]. A nonlinear AHE has recently been demonstrated in a few-layer nonmagnetic WTe₂ under an angle-resolved electrical measurement [28]. Despite numerous reports, the underlying mechanism behind the anomalous enhancement in Hall conductivity is still an open question. Additionally, no generalized method is available as of now that can predict the AHE nature of FM vdW heterostructures under a tunable Berry-curvature distribution.

Here, we propose a generalized mechanism for the fundamental origin of enhanced AHC in the CrS₂/CrBr₃ vdW heterostructure. Using symmetry arguments and first-principles calculations, we show that the proximity-induced exchange interaction carries an identical nature of spin magnetic moment from magnetic CrBr₃ to nonmagnetic CrS₂ layer. The induced out-of-plane magnetization and orbital magnetic moments in the CrS₂ layer lead to an additional contribution to Berry-curvature induced AHC. Based on tight-binding analysis, we reveal a strong correlation between AHE and proximity interaction. Interestingly, in the CrS₂ layer,

^{*}Contact author: abhishek@iisc.ac.in

the angular profiles of induced magnetization and AHC are identical to magnetic moment variation in CrBr_3 . Competition between magnetic proximity interactions and SOC results in such angular profiles. The observed results offer a potential approach for predicting AHC variations in valley-polarized heterostructures through symmetry-assisted MPE.

II. COMPUTATIONAL METHODS

In order to understand the valley polarization in the $\text{CrS}_2/\text{CrBr}_3$ vdW heterostructure, the first-principles calculations are carried out by spin-polarized density functional theory (DFT) as implemented in the Vienna *ab initio* Simulation Package (VASP) [29,30]. The all-electron projector augmented wave (PAW) potentials are used to describe the ion-electron interactions in the system [31,32]. The electronic exchange-correlation potentials are represented by the Perdew-Burke-Ernzerhof (PBE) [33] generalized gradient approximation (GGA). The plane wave basis sets with the energy cutoff of 500 eV are used to expand the single-particle eigenstates of the Kohn-Sham equations. A well-converged Γ -centered Monkhorst-Pack [34] k grid of $15 \times 15 \times 1$ is adapted to sample the BZ of CrS_2 , CrBr_3 monolayers and the $\text{CrS}_2/\text{CrBr}_3$ heterostructure. The vdW heterostructure and monolayers are fully relaxed with the conjugate gradient algorithm until the Hellmann-Feynman forces acting on each ion are less than 0.005 eV/\AA . A vacuum of 20 \AA is used to avoid the interactions between periodic images along the z axis in the monolayers and heterostructure. The weak vdW interaction between the layers in the heterostructure is incorporated by Grimme's PBE-D2 [35], where a pairwise force field represents the weak vdW interactions. The strong on-site Coulombic interaction of d orbitals of Cr atoms in the magnetic layer of monolayers and the heterostructure is considered using a Hubbard-like effective U parameter [36] of value $U_{\text{eff}} = U - J = 4 \text{ eV}$, $U = 4 \text{ eV}$, and $J = 0 \text{ eV}$ [37]. For all the calculations, spin polarization is explicitly considered for monolayers and the heterostructure. The SOC is incorporated in the noncollinear approach as implemented in VASP. The phonon dispersions of monolayers are calculated using the density functional perturbation theory (DFPT) [38] using $2 \times 2 \times 1$ supercells. The phonon frequencies are extracted by the PHONOPY package [39] based on the Parlinski-Li-Kawazoe method. The lattice mismatch has been defined by

$$\eta = \frac{|a_1 - a_2|}{a_1} \times 100\%,$$

where a_1 and a_2 are the lattice constants for different layers in the heterostructures.

Wannier calculations

In order to obtain detailed information about valley polarization, a Wannier-function-based tight-binding model is developed using the real-space maximally localized Wannier functions (MLWFs) as implemented in the WANNIER90 package [40]. The MLWFs are constructed based on the initial orbital projections of d orbitals of Cr atoms and p orbitals of S and Br atoms, respectively. Further, the WANNIERTOOLS [41] is used for calculating the Berry curvature [$\Omega(\mathbf{k})$] and

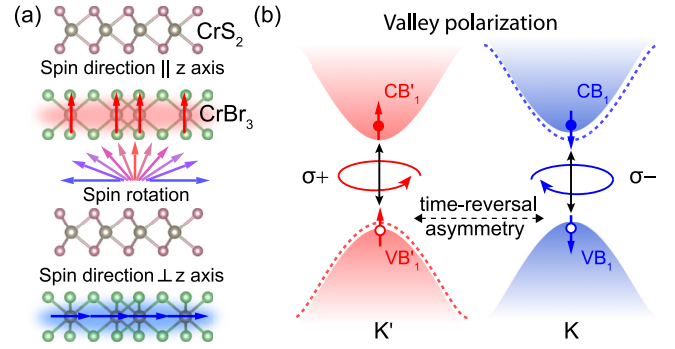


FIG. 1. (a) The $\text{CrS}_2/\text{CrBr}_3$ heterostructure with an out-of-plane and in-plane spin orientation of Cr atoms in magnetic layer. Arrows represent the spin orientation from -90° to $+90^\circ$ in yz plane. (b) Schematic of energy diagram depicting the K/K' valley degeneracy (dotted parabola vs shaded parabola) and valley degeneracy lifting (shaded parabola vs shaded parabola). $\sigma+$ and $\sigma-$ represent the interband optical transition for right- and left-handed circularly polarized lights, respectively.

anomalous Hall conductivity (AHC) of monolayers and heterostructures. A sufficiently large k grid of $100 \times 100 \times 1$ in the first BZ is considered to calculate the $\Omega(\mathbf{k})$. The Kubo formalism has been used to simulate Berry curvature [42,43] as given by

$$\Omega(\mathbf{k}) = \sum_n f_{nk} \Omega_n(\mathbf{k}), \quad (1)$$

where

$$\Omega_n(\mathbf{k}) = \sum_{m \neq n} \frac{2\text{Im} \langle \psi_{nk} | v_x | \psi_{mk} \rangle \langle \psi_{mk} | v_y | \psi_{nk} \rangle}{(E_m - E_n)^2}. \quad (2)$$

Here, f_n is the Fermi-Dirac distribution function, where n is the occupied states of the system. u_{nk} and E_n are the periodic part of the Bloch wave associated with the n th band and eigenvalue of Bloch functions ψ_{nk} , respectively. v_x and v_y are the velocity operators. The AHC σ_{xy} can be obtained by integrating $\Omega_n(\mathbf{k})$ over the first BZ of the system [44] as given by

$$\sigma_{xy} = -\frac{e^2}{\hbar} \int_{\text{BZ}} \frac{d\mathbf{k}}{(2\pi)^2} \Omega_n, \quad (3)$$

where e is electronic charge and \hbar is the reduced Planck's constant.

III. RESULTS AND DISCUSSION

Energetically, the most stable stacking order (AB stacking) of $\text{CrS}_2/\text{CrBr}_3$ vdW heterostructure is shown in Fig. 1(a), constructed using fully relaxed $2H$ CrS_2 and CrBr_3 monolayers. A comparison between the ground state energies of $2H$ and $1T$ phases of the optimized CrS_2 monolayers [45,46] is given in Table S1 of the Supplemental Material (SM) [53]. The ground state energy of the $2H$ phase is $\sim 4.2 \text{ meV/unit cell}$ lower than the $1T$ phase. This indicates that the $2H$ phase is more stable than the $1T$ phase in our calculations, consistent with previous reports [47–50]. However, both the structures are experimentally feasible [51]. Therefore, before selecting

between the $2H$ and $1T$ CrS_2 crystal structures, our prime concern was determining whether the system lacked \mathcal{I} . The crystal symmetry of $2H$ CrS_2 is D_{3h} , which indicates that \mathcal{I} is explicitly broken. On the other hand, the space group of $1T$ CrS_2 is $P\bar{3}m1$. As a result, \mathcal{I} is preserved in the $1T$ phase, limiting its valleytronics applications. Therefore, we consider the $2H$ phase over the $1T$ phase of CrS_2 for this work, which agrees well with previous studies [52]. Details of stability, structural, and electronic properties are discussed in Secs. 1–4 (Figs. S1–S5 and Tables S1–S2) of SM [53] (see also Refs. [54–59] therein). The CrBr_3 layer in the heterostructure possesses out-of-plane FM ordering [top panel of Fig. 1(a)] consistent with previous studies [60,61]. Manipulation of this magnetic moment direction in the FM vdW heterostructure is well established by theoretical studies with an experimental verification [22,26]. A schematic representation of the in-plane magnetization direction of each Cr atom in the CrBr_3 layer is shown in the bottom panel of Fig. 1(a).

The electronic band structure of the $\text{CrS}_2/\text{CrBr}_3$ vdW heterostructure [Fig. S5(a)] reflects the presence of a strong SOC in the system. The valence band (VB) [conduction band (CB)] at the K valley splits into two subbands, VB_1 and VB_2 (CB_1 and CB_2), which originate from the CrS_2 layer in the heterostructure. Similarly, at the K' valley, they split into VB'_1 and VB'_2 (CB'_1 and CB'_2). This valley spin splitting can be described by the Hamiltonian $\hat{H}_{SO} = \frac{1}{2}\sigma \cdot \omega(\mathbf{k})$ [23,62], where σ are Pauli spin matrices and $\omega(\mathbf{k})$ is the Larmor frequency of electron spin associated with intrinsic k -dependent magnetic field $B_i(\mathbf{k})$. A similar spin splitting is observed in the VB and CB of the isolated CrS_2 monolayer [Fig. S5(b)]. This spin splitting at valleys occurs due to the presence of d orbitals of heavy Cr atoms and breaking of \mathcal{I} in monolayers as well as the heterostructure. As a result, the CrS_2 monolayer exhibits a nonzero Berry curvature $\Omega_z(\mathbf{k}) [= \hat{\mathbf{z}} \cdot \langle u_n(\mathbf{k}) | i\nabla_k | u_n(\mathbf{k}) \rangle]$, where $|u_n(\mathbf{k})\rangle$ is the periodic part of the Bloch function] at the K/ K' valleys [Fig. S6(e)]. The opposite sign of $\Omega_z(\mathbf{k})$ at the K/ K' valleys represents the chirality-associated valley states resulting in the optical circular dichroism phenomenon [5,63–65], as shown in Fig. 1(b).

Furthermore, the spin splitting observed at the K and K' valleys is the fundamental source for experimentally measured VHE upon electron/hole doping. To get physical insight into this spin splitting, we consider the $\mathbf{k} \cdot \mathbf{p}$ model with SOC using symmetry-adapted basis functions for two valleys, $|\psi_c\rangle = |d_z^2\rangle$, $|\psi_v^\tau\rangle = \frac{1}{\sqrt{2}}(|d_{x^2-y^2}\rangle + i\tau|d_{xy}\rangle)$ ($\tau = \pm 1$ are valley indices). The model Hamiltonian is given as [5]

$$\hat{H}_1 = at(\tau k_x \hat{\sigma}_x + k_y \hat{\sigma}_y) + \frac{\Delta}{2} \hat{\sigma}_z - \lambda \tau \frac{\hat{\sigma}_z - 1}{2} \hat{s}_z, \quad (4)$$

where a , t , Δ , $\hat{\sigma}$, 2λ , and \hat{s}_z are lattice constant, effective hopping integral, band gap, Pauli matrices, spin splitting, and Pauli spin matrix, respectively. Zoomed versions of valley splitting in VB edge for the CrS_2 monolayer using DFT and the $\mathbf{k} \cdot \mathbf{p}$ model are shown in Figs. S6(a) and S6(b), respectively. The value of spin splitting using DFT for monolayers is 68.7 meV at both the K and K' valleys, comparable to other TMDCs [5]. The SOC term in \hat{H}_1 qualitatively captures the information of valley splitting similar to that expected from \hat{H}_{SO} [Fig. S6(b)]. Notably, equal and opposite spin splitting observed at distinct valleys suggests the invariance of \mathcal{T} in

monolayers [dotted parabola vs shaded parabola in Fig. 1(a)]. It could be compared with the zero energy difference (ΔE_σ) in optical pumping energies between right (σ^+) and left (σ^-) handed polarizations in circular dichroism experiments. However, opposite but unequal spin splittings of 71.4 and 66.6 meV are observed at the K and K' valleys, respectively, for the $\text{CrS}_2/\text{CrBr}_3$ vdW heterostructure [Fig. 2(a)]. This is a direct consequence of breaking \mathcal{T} along with \mathcal{I} , which lifts the Kramers spin degeneracy at K and K' , resulting in valley polarization in the heterostructure. The valley polarization at VB (CB) is found to be $\Delta_{VB} = \text{VB}_1 - \text{VB}'_1 = 2.4$ meV ($\Delta_{CB} = \text{CB}_1 - \text{CB}'_1 = -2.3$ meV). As there is a direct correlation of \mathcal{T} with magnetic field, the origin of the shift can be associated with magnetic moments in the magnetic layer. To investigate that we include the Zeeman term in Hamiltonian \hat{H}_1 [66,67]:

$$\hat{H}_2 = \hat{H}_1 + \frac{\hat{\sigma}_z - 1}{2} (\hat{s}_z + \tau\alpha)B, \quad (5)$$

where the effective exchange field $B = (\Delta_{VB} + \Delta'_{VB})/4$ and orbital magnetic moment $\alpha = (\Delta_{VB} - \Delta'_{VB})/(\Delta_{VB} + \Delta'_{VB})$ with $\Delta'_{VB} = \text{VB}'_2 - \text{VB}_2 = 2.3$ meV are obtained from DFT. The calculated band dispersions around K and K' in VB using \hat{H}_2 are shown in Fig. 2(b), where valley degeneracy lifting is clearly captured [similar to the DFT result, given in Fig. 2(a)]. The valley splittings in VB at K and K' from the $\mathbf{k} \cdot \mathbf{p}$ model are 71.0 and 66.59 meV, respectively. The corresponding valley polarizations are $\Delta_{VB} = 2.44$ meV ($\Delta_{CB} = -2.32$ meV), close to DFT result. For $\text{CrS}_2/\text{CrBr}_3$ heterostructure ΔE_σ is 4.76 meV ($= \Delta_{VB} - \Delta_{CB}$) which enables optical polarization of charge carriers [63]. Therefore, the Zeeman term in \hat{H}_2 well captures the information of valley polarization, indicating the presence of magnetization in the CrS_2 layer.

As expected, the magnetic moment of the CrBr_3 layer per Cr atom is $\sim 3.32 \mu_B$ in the heterostructure, similar to the CrBr_3 monolayer ($\sim 3.02 \mu_B$ per Cr atom). The CrS_2 layer exhibits a nonvanishing magnetic moment of $0.03 \mu_B$ per Cr atom after adding the magnetic substrate. In order to find the origin of this magnetization in the nonmagnetic CrS_2 layer, the atom-resolved charge density and magnetic moment have been calculated. The planar average charge densities along the z direction (ρ_z) for VB_1 (VB'_1) at K (K') are shown in Fig. 2(c), where two different triple color strips indicate the contribution of each layer. From ρ_z , it is found that VB_1 (VB'_1) is solely contributed by Cr atoms of the CrS_2 layer. Moreover, the induced magnetic moment is localized at Cr atoms of the CrS_2 layer (at VB_1 and VB'_1 bands) and is oriented along z (out-of-plane; $\mathbf{B} \neq 0$ and $\hat{\mathbf{s}} \parallel \hat{\mathbf{z}}$) direction. This is due to out-of-plane spin orientation of Cr atoms in the magnetic CrBr_3 layer. To ensure whether out-of-plane magnetization is the actual cause for valley polarization or not, we next align the spins along the y (in-plane) direction for each Cr atom in the CrBr_3 layer. The finite spin splitting is also observed for in-plane spin orientation at the K and K' valleys as shown in Fig. 2(d). The DFT calculations show a spin splitting of 69.10 meV for both valleys, leading to zero valley polarization [Fig. 2(e)]. The DFT results are consistent with model predictions even without the presence of the Zeeman term, suggesting absence of an induced magnetic moment in the nonmagnetic layer. The Cr atom in the CrS_2 layer acquires an in-plane (along y)

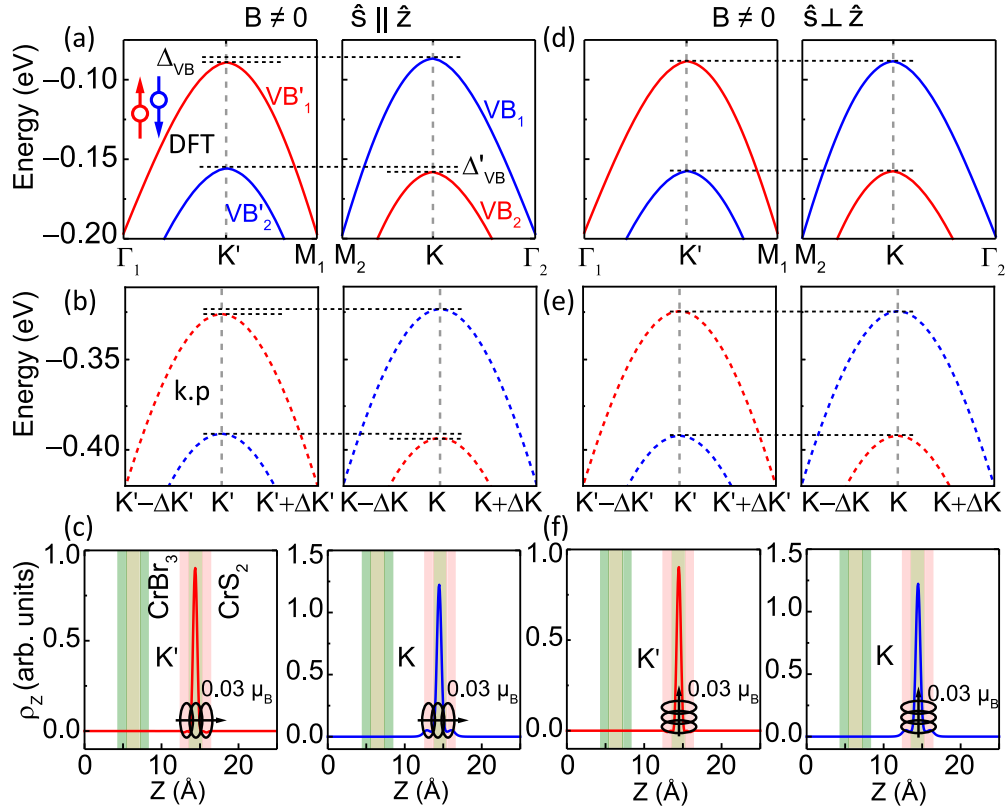


FIG. 2. The zoom-in plot of VB edges around K/K' and with MPE for CrS₂/CrBr₃ heterostructure with out-of-plane spin orientation from (a) DFT and (b) $\mathbf{k} \cdot \mathbf{p}$ model. (c) Planar average charge density along z direction at K' and K, indicating the induced magnetic moments in CrS₂ layer are oriented along z direction. The VB edges around K' and K for in-plane spin orientation from (d) DFT and (e) $\mathbf{k} \cdot \mathbf{p}$ model. (f) Planar average charge density along the y direction of VB edges at K' and K, indicating the induced magnetic moments in CrS₂ layer are oriented along y direction.

induced magnetic moment ($0.03 \mu_B$) similar to the out-of-plane spin orientation as shown in Fig. 2(f). Notably, in-plane magnetization does not lift valley spin degeneracy within the heterostructure. Therefore, out-of-plane magnetization is the sole reason for lifting of valley degeneracy. Additionally, we found a strong dependence of valley polarization on different on-site interactions ($U = 2, 3, 4$) with $\hat{s} \parallel \hat{z}$ (see SM [53] for details), which further justifies this observation.

In order to get better insights, a detailed symmetry analysis associated with the valley-splitting phenomenon is carried out. The out-of-plane mirror symmetry \mathcal{M}_Z is preserved in the CrS₂ monolayer, as shown in Fig. S6(c). However, as the CrS₂ layer is placed on the magnetic CrBr₃ layer, along with the crystal symmetry, magnetic space group symmetry also comes into the picture. As discussed, the spin orientation of induced magnetization in the CrS₂ layer is similar to that in the CrBr₃ layer. For a system with mirror symmetry, the spins perpendicular to the mirror plane remain the same; however, spins parallel to the plane should be flipped on either side of the mirror plane [68]. Therefore, if \mathcal{M}_Z in the heterostructure corresponds to an intermediate mirror plane between CrS₂ and CrBr₃ layers, then \mathcal{M}_Z will be preserved in the system for $\hat{s} \parallel \hat{z}$ in the CrBr₃ layer. A similar concept is also introduced by Zhang *et al.* for the antiferromagnetic bilayer [69]. On the other hand, in the case of $\mathbf{B} \neq 0$ and $\hat{s} \perp \hat{z}$, both \mathcal{M}_Z and \mathcal{T} are individually broken along the Γ -K (K') directions in

the CrS₂ layer, while the system remains invariant under joint operation [69] of \mathcal{T} and \mathcal{M}_Z protecting spin degeneracy at the K/K' valleys for $\hat{s} \perp \hat{z}$. However, for $\mathbf{B} \neq 0$ and $\hat{s} \parallel \hat{z}$, although \mathcal{T} is broken, due to preservation of \mathcal{M}_Z the system would no longer be invariant under the joint symmetry operation of \mathcal{T} and \mathcal{M}_Z , resulting in a finite valley polarization. To understand the nature of the MPE and associated valley polarization in the CrS₂ layer, spins within the magnetic layer are rotated from -90° to $+90^\circ$ in the yz plane [Fig. 1(a)]. The magnetic anisotropy energy is quite low (≤ 0.1 meV/unit cell). The electronic band dispersions around the K and K' valleys (zoom-in plot) for each spin angle from -15° to $+15^\circ$ are shown in Figs. S7 and S8. The corresponding valley polarizations for VB (Δ_{VB}) and CB (Δ_{CB}) are shown in Fig. 3(a). It is observed that Δ_{VB} (Δ_{CB}) follows the cosine-like variation with spin orientation. The ideal cosine functions (solid blue lines for positive values and dotted blue lines for negative values) are plotted for guidance and to measure the deviation of actual data. The Δ_{VB} (Δ_{CB}) reaches the maximum of 3.2 meV (-3.2 meV) at -15° and a minimum of zero meV (-0.1 meV) at $\pm 90^\circ$, providing an ideal way to control the valley degree of freedom via spin orientation.

To identify the origin of cosine-like variation of $\Delta_{VB(CB)}$, the average magnetic moment (M') of CrS₂ layer is computed. The M' shares similar characteristics as $\Delta_{VB(CB)}$ [Fig. 3(b)] with a maximum value at -15° . This peak value causes the

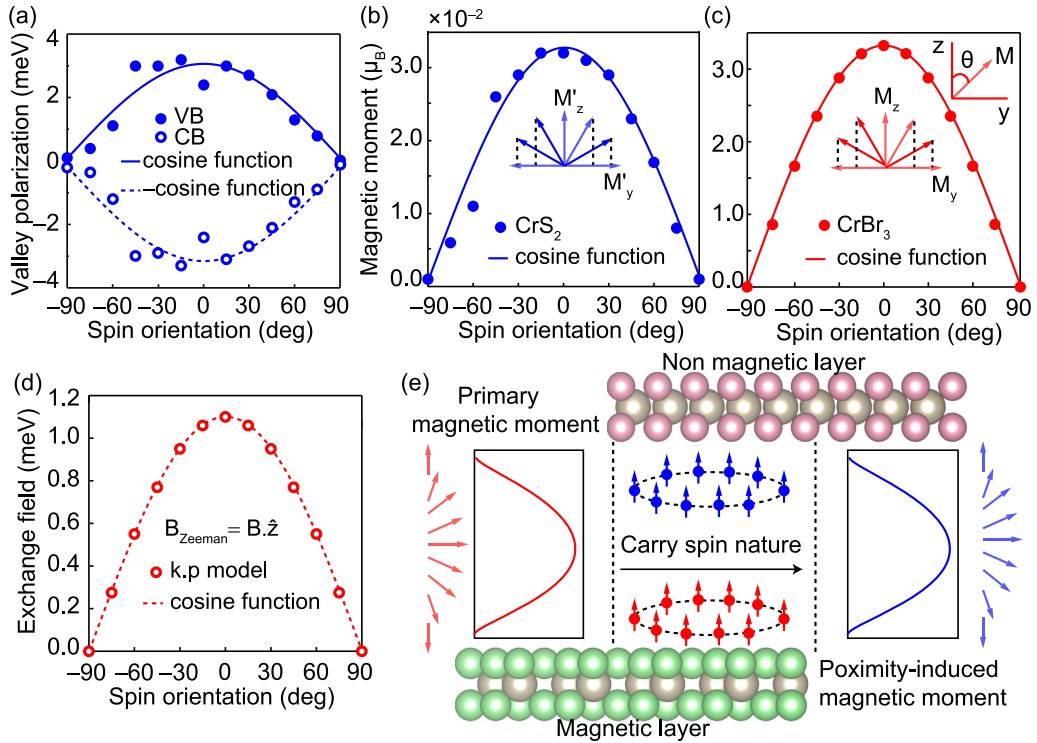


FIG. 3. (a) Valley polarization at VB (solid blue circle) and CB (hollow blue circle) in heterostructure as a function of the spin orientation of Cr atoms in CrBr₃ layer. Average values of (b) induced magnetic moment of Cr atoms in the CrS₂ layer, (c) magnetic moment of Cr atoms in CrBr₃ layer as a function of spin orientation. θ is the angle made by magnetic moment \mathbf{M} with z axis in CrBr₃ layer. (d) The calculated value of out-of-plane exchange field from $\mathbf{k} \cdot \mathbf{p}$ model as a function of spin orientation. (e) Schematic depicts the carrying of similar nature of spin magnetic moment to nonmagnetic CrS₂ layer with spin orientation in CrBr₃ layer via MPE.

valley polarization to reach its maximum value at -15° . The origin of maximum valley polarization at -15° can be understood from the concept of orbital magnetic moment at valleys. It is shown by Xiao *et al.* that the orbital magnetic moment at the K/K' valleys is inversely proportional to the effective mass of electrons (m_e^*) [70]. We, therefore, calculated the m_e^* from band dispersion of the VBM of the heterostructure at the K/K' valleys. The calculated ratio of m_e^* at -15° and 0° is $\frac{m_e^*(-15^\circ)}{m_e^*(0^\circ)} = 0.9735 < 1$. Similarly, for other spin angles, m_e^* values are higher compared to -15° , suggesting the highest orbital magnetic moment at -15° . Again, from the layer-resolved band structure of the CrS₂/CrBr₃ heterostructure (Fig. S5(a) in SM [53]), it is found that the VBM at the K/K' valleys is mainly contributed by the CrS₂ layer. This indicates that the orbital magnetic moments at valleys are induced magnetic moments. As a result, the CrS₂ layer exhibits a maximum induced magnetic moment, which in turn leads to a maximum valley polarization at -15° instead of 0° .

In order to understand the cosine-like nature of M' in the CrS₂ layer, the average magnetic moment of the CrBr₃ layer is calculated. Interestingly, a similar trend is also found in the CrBr₃ layer [Fig. 3(c)], suggesting a possible proximity effect where the CrBr₃ layer induces the cosine-like behavior in the nonmagnetic CrS₂ layer. For further verification, we consider an out-of-plane exchange field $B_{ex} (= \mathbf{B} \cdot \hat{\mathbf{z}})$ in Eq. (5) to couple to spins in the CrS₂ layer for each magnetization direction. The Hamiltonian with the exchange term is as

follows,

$$\hat{H}_3 = \begin{pmatrix} \frac{\Delta}{2} & at(\tau k_x - ik_y) \\ at(\tau k_x + ik_y) & -\frac{\Delta}{2}\hat{\sigma}_z + \lambda\tau\hat{s}_z - (\hat{s}_z + \tau\alpha)B_{ex} \end{pmatrix}. \quad (6)$$

The out-of-plane B_{ex} for each spin angle is calculated from \hat{H}_3 , which is shown in Fig. 3(d). The cosine-like variation of B_{ex} confirms that the MPE originating from the magnetic layer is responsible for the cosine-like behavior of the induced magnetic moment as well as the valley polarization in the CrS₂ layer. Our results strongly suggest that the proximity-induced exchange field carries a similar pattern of spin moments from the magnetic to nonmagnetic layer via the MPE [Fig. 3(e)], providing important insight into valleytronics experiments.

To observe the impact of this unique characteristic of the MPE on valley Hall transport, we further analyze the symmetries associated with valley degrees of freedom. The breaking of \mathcal{I} results in nonzero $\Omega_z(\mathbf{k})$ in CrS₂/CrBr₃ vdW heterostructure as shown in Fig. 4(a). The 2D $\Omega_z(\mathbf{k})$ for $\hat{\mathbf{s}} \perp \hat{\mathbf{z}}$ and $\hat{\mathbf{s}} \parallel \hat{\mathbf{z}}$ shows that spin-up and spin-down states contribute $\Omega_z(\mathbf{k})$ at the K' and K valleys, respectively. It indicates the presence of both out-of-plane and in-plane magnetization in the CrS₂ layer. This is the opposite scenario to $B = 0$ (Figs. S11(a)–S11(c) in SM [53]), where \mathcal{I} is broken while \mathcal{T} is preserved, resulting in $\Omega_z(\mathbf{k}) = -\Omega_z(-\mathbf{k})$. As a result, Bloch electrons at the K and K' valleys acquire an anomalous velocity

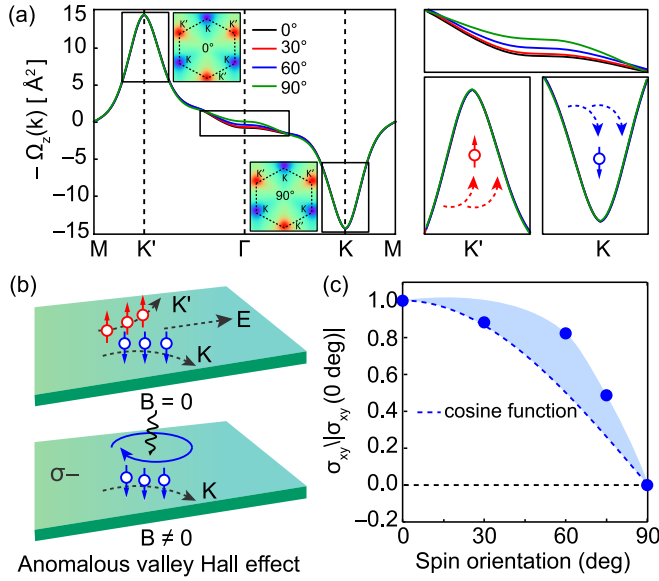


FIG. 4. (a) 1D $\Omega_z(\mathbf{k})$ for positive spin angles. Inset represents the contour map of 2D $\Omega_z(\mathbf{k})$ for spin angles 0° and 90° for heterostructure. The right-side top panel shows a zoomed version of the variation of 1D $\Omega_z(\mathbf{k})$ around Γ point, and bottom panel shows the direction of \mathbf{v}_a of spin-up and spin-down holes. The blue (red) hollow circles depict holes in K (K') valleys, and blue (red) arrows depict spin-down (spin-up) directions. (b) The upper schematic represents VHE in monolayer CrS_2 with hole doping without MPE. The lower schematic represents AVHE in heterostructure with hole doping with MPE. The complete spin polarization occurs at K valley by applying left-circularly polarized light. (c) The blue solid circles represent the spin-angle dependence of AHC relative to σ_{xy} at 0° at $E = E_F$. The blue-colored area highlights the deviation from ideal cosine function.

$\mathbf{v}_a \sim \mathbf{E} \times \Omega_z(\mathbf{k})$ [44] and move along opposite directions in the presence of an in-plane electric field \mathbf{E} [Fig. 4(b), top panel]. However, for the heterostructure, due to simultaneous breaking of \mathcal{T} and \mathcal{I} , the spin-down holes from the K valley move to the bottom boundary with 100% spin polarization. This gives rise to the anomalous valley Hall effect (AVHE) [Fig. 4(b), bottom panel], leading to a static net Hall current, hence a nonzero AHC (σ_{xy}) in the heterostructure.

On the other hand, for the nonmagnetic CrS_2 monolayer $[\hat{H}_1, \mathcal{T}] = 0$ results in vanishing AHC. The normalized σ_{xy} [$\sigma_{xy}/|\sigma_{xy}(0^\circ)|$] in the proximitized CrS_2 layer for different spin orientation has been computed using the Wannier-function-based tight-binding model (see SM [53]). For spin-angle $0^\circ \leq \theta < 90^\circ$, the proximity-induced magnetism lifts the Kramers degeneracy, resulting in nonzero σ_{xy} . The nonzero σ_{xy} leads to an additional contribution to intrinsic Hall conductivity of monolayer, implying an enhancement in AHC in the CrS_2 layer. For the in-plane magnetization direction ($\theta = 90^\circ$), both \mathcal{T} and \mathcal{M}_Z are broken in the heterostructure. However, preservation of their joint symmetry operation protects the Kramers degeneracy in the entire BZ, leading to vanishing AHE. To understand the reason behind this vanishing σ_{xy} we investigate the effect of the joint symmetry operation of \mathcal{T} and \mathcal{M}_Z on the anomalous velocity \mathbf{v}_a . It can be shown that \mathbf{v}_a , \mathbf{k} , and \mathbf{E} have even parities under out-of-plane mirror reflection \mathcal{M}_Z [71]. Under such conditions,

one could obtain $\mathbf{v}_a(\mathbf{k}) \sim \mathbf{E} \times \Omega_z(\mathbf{k})$, while they have odd parity under time-reversal operation \mathcal{T} , resulting in $-\mathbf{v}_a(-\mathbf{k}) \sim -\mathbf{E} \times \Omega_z(-\mathbf{k})$. To ensure the system remains invariant under the combined operation of \mathcal{T} and \mathcal{M}_Z , the left-handed sides of these two equations should satisfy the condition $\mathbf{v}_a(-\mathbf{k}) = -\mathbf{v}_a(\mathbf{k})$. This further suggests that $\Omega_z(\mathbf{k}) = -\Omega_z(-\mathbf{k})$. As a result, the AHC obtained by integrating over the first BZ, i.e., $\sigma_{xy} = -\frac{e^2}{h} \int_{BZ} \frac{d\mathbf{k}}{(2\pi)^2} \Omega_z(\mathbf{k})$, becomes zero.

Figure 4(c) represents the spin angle dependence of σ_{xy} , calculated from band structures of $\text{CrS}_2/\text{CrBr}_3$ heterostructure. The σ_{xy} decreases following the cosine nature as the out-of-plane spin component is tilted toward the in-plane direction. The light-blue-colored area highlights the deviation of normalized σ_{xy} at $E = E_F$ from the ideal cosine function. To get insight into this AHC nature, we apply the semiclassical formulation of wave packet dynamics of Bloch electrons [70,72]. It is found that in addition to the spin magnetic moment, Bloch electrons carry an orbital magnetic moment, given by $m(\mathbf{k}) = -i\frac{e}{2\hbar} \langle \nabla_k u | [\hat{H}(\mathbf{k}) - \epsilon(\mathbf{k})] | \nabla_k u \rangle$, where $\hat{H}(\mathbf{k})$ is the Bloch Hamiltonian and $\epsilon(\mathbf{k})$ is the band energy. The orbital moment, together with a correction from Berry curvature, results in valley-contrasting orbital magnetization $\mathbf{M}' = -2 \int \frac{d\mathbf{k}}{(2\pi)^2} \{m(\mathbf{k}) + \frac{e}{\hbar} [\mu - \epsilon(\mathbf{k})] \Omega(\mathbf{k})\}$ [70], which causes a population imbalance at valleys. The average \mathbf{M}' in the CrS_2 layer decreases with the increase in spin angle, as shown in Fig. 3(b). This implies the corrections from $\Omega(\mathbf{k})$ becoming smaller as the spin moments are aligned toward the in-plane direction. This can be directly observed from Fig. 4(a) (right-side top panel), where one-dimensional (1D) $\Omega_z(\mathbf{k})$ decreases along Γ - K (K') with spin orientation. This, in turn, leads to a reduction in the anomalous velocities of Bloch electrons at band edges. As a result, the AHC decreases as well with an increase in spin angles, following $\Omega_z(\mathbf{k}) = [\hat{\mathbf{z}} \cdot \Omega(\mathbf{k})]$, hence following \mathbf{M}' . This clarifies that the σ_{xy} within the heterostructure has the same characteristic as valley orbital magnetization in the CrS_2 layer. The observed result opens up a direction to understand the AVHE nature under a tunable spin Berry curvature by analyzing the MPE.

IV. CONCLUSIONS

In conclusion, using symmetry arguments and tight-binding analysis, we unveil the origin of the significantly enhanced AHC in the CrS_2 layer in the $\text{CrS}_2/\text{CrBr}_3$ vdW heterostructure. We show that MPE induces a similar cosine-like nature of magnetic moments from the CrBr_3 to CrS_2 layer. This induced magnetization leads to an additional contribution to Berry-curvature-induced AHC for out-of-plane magnetization directions. Furthermore, a strong correlation has been established between AHC and MPE. The MPE induces an angular profile of σ_{xy} in the CrS_2 layer, similar to the magnetic moment variation in the CrBr_3 layer. These findings offer an approach to predict the variation of σ_{xy} in a nonmagnetic layer in a valley-polarized heterostructure through the symmetry-assisted MPE.

ACKNOWLEDGMENTS

The authors thank the Materials Research Center (MRC), Solid State Structural and Chemistry Unit (SSCU), and

Supercomputer Education and Research Center (SERC), Indian Institute of Science, for providing the computational facilities. The authors acknowledge support from the DST-Naomisson program of the Department of Science and Technology, Government of India (Grant No.

DST/NM/TUE/QM-1/2019). The authors thank Ch. Uma Lavanaya for her useful suggestions in model calculations. The authors are thankful to Ashutosh Srivastava and Shibu Meher for their useful comments on manuscript writing.

-
- [1] J. R. Schaibley, H. Yu, G. Clark, P. Rivera, J. S. Ross, K. L. Seyler, W. Yao, and X. Xu, Valleytronics in 2D materials, *Nat. Rev. Mater.* **1**, 16055 (2016).
- [2] X. Xu, W. Yao, D. Xiao, and T. F. Heinz, Spin and pseudospins in layered transition metal dichalcogenides, *Nat. Phys.* **10**, 343 (2014).
- [3] S. H. Gong, I. Komen, F. Alpeggiani, and L. Kuipers, Nanoscale optical addressing of valley pseudospins through transverse optical spin, *Nano Lett.* **20**, 4410 (2020).
- [4] V. Pandey, S. Mishra, N. Maity, S. Paul, A. K. Roy, N. R. Glavin, K. Watanabe, T. Taniguchi, A. K. Singh, and V. Kochat, Probing interlayer interactions and commensurate-incommensurate transition in twisted bilayer graphene through Raman spectroscopy, *ACS Nano* **18**, 4756 (2024).
- [5] D. Xiao, G. B. Liu, W. Feng, X. Xu, and W. Yao, Coupled spin and valley physics in monolayers of MoS₂ and other group-VI dichalcogenides, *Phys. Rev. Lett.* **108**, 196802 (2012).
- [6] S. Sinha, P. C. Adak, R. S. Surya Kanthi, B. L. Chittari, L. D. V. Sangani, K. Watanabe, T. Taniguchi, J. Jung, and M. M. Deshmukh, Bulk valley transport and Berry curvature spreading at the edge of flat bands, *Nat. Commun.* **11**, 5548 (2020).
- [7] M. Ezawa, Valley-polarized metals and quantum anomalous Hall effect in silicene, *Phys. Rev. Lett.* **109**, 055502 (2012).
- [8] M. Tahir, A. Manchon, K. Sabeeh, and U. Schwingenschlogl, Quantum spin/valley Hall effect and topological insulator phase transitions in silicene, *Appl. Phys. Lett.* **102**, 162412 (2013).
- [9] C. J. Tabert and E. J. Nicol, ac/dc spin and valley Hall effects in silicene and germanene, *Phys. Rev. B* **87**, 235426 (2013).
- [10] F. Zhan, B. Zheng, X. Xiao, J. Fan, X. Wu, and R. Wang, Magnetic field induced valley-polarized quantum anomalous Hall effects in ferromagnetic van der Waals heterostructures, *Phys. Rev. B* **105**, 035131 (2022).
- [11] A. Rycerz, J. Tworzydło, and C. W. J. Beenakker, Valley filter and valley valve in graphene, *Nat. Phys.* **3**, 172 (2007).
- [12] K. Behnia, Polarized light boosts valleytronics, *Nat. Nanotechnol.* **7**, 488 (2012).
- [13] Y. Li, J. Ludwig, T. Low, A. Chernikov, X. Cui, G. Arefe, Y. D. Kim, A. M. van der Zande, A. Rigosi, H. M. Hill, S. H. Kim, J. Hone, Z. Li, D. Smirnov, and T. F. Heinz, Valley splitting and polarization by the Zeeman effect in monolayer MoSe₂, *Phys. Rev. Lett.* **113**, 266804 (2014).
- [14] A. Srivastava, M. Sidler, A. V. Allain, D. S. Lembke, A. Kis, and A. Imamoglu, Valley Zeeman effect in elementary optical excitations of monolayer WSe₂, *Nat. Phys.* **11**, 141 (2015).
- [15] G. Aivazian, Z. Gong, A. M. Jones, R. L. Chu, J. Yan, D. G. Mandrus, C. Zhang, D. Cobden, W. Yao, and X. Xu, Magnetic control of valley pseudospin in monolayer WSe₂, *Nat. Phys.* **11**, 148 (2015).
- [16] A. Ramasubramanian and D. Naveh, Mn-doped monolayer MoS₂: An atomically thin dilute magnetic semiconductor, *Phys. Rev. B* **87**, 195201 (2013).
- [17] R. Mishra, W. Zhou, S. J. Pennycook, S. T. Pantelides, and J. C. Idrobo, Long-range ferromagnetic ordering in manganese-doped two-dimensional dichalcogenides, *Phys. Rev. B* **88**, 144409 (2013).
- [18] Q. Zhang, S. A. Yang, W. Mi, Y. Cheng, and U. Schwingenschlogl, Large spin-valley polarization in monolayer MoTe₂ on top of EuO(111), *Adv. Mater.* **28**, 959 (2016).
- [19] Z. Zhang, X. Ni, H. Huang, L. Hu, and F. Liu, Valley splitting in the van der Waals heterostructure WSe₂/CrI₃: The role of atom superposition, *Phys. Rev. B* **99**, 115441 (2019).
- [20] C. Zhao, T. Norden, P. Zhang, P. Zhao, Y. Cheng, F. Sun, J. P. Parry, P. Taheri, J. Wang, Y. Yang, T. Scrace, K. Kang, S. Yang, G.-x. Miao, R. Sabirianov, G. Kioseoglou, W. Huang, A. Petrou, and H. Zeng, Enhanced valley splitting in monolayer WSe₂ due to magnetic exchange field, *Nat. Nanotechnol.* **12**, 757 (2017).
- [21] S. Sattar, J. A. Larsson, C. M. Canali, S. Roche, and J. H. Garcia, Giant valley-polarized spin splittings in magnetized Janus Pt dichalcogenides, *Phys. Rev. B* **105**, L041402 (2022).
- [22] T. Hu, G. Zhao, H. Gao, Y. Wu, J. Hong, A. Stroppa, and W. Ren, Manipulation of valley pseudospin in WSe₂/CrI₃ heterostructures by the magnetic proximity effect, *Phys. Rev. B* **101**, 125401 (2020).
- [23] B. Scharf, G. Xu, A. Matos-Abiague, and I. Zutic, Magnetic proximity effects in transition-metal dichalcogenides: Converting excitons, *Phys. Rev. Lett.* **119**, 127403 (2017).
- [24] J. Li, L. Gu, and R. Wu, Possible realization and protection of valley-polarized quantum Hall effect in MnWS₂, *Phys. Rev. B* **101**, 024412 (2020).
- [25] T. Habe and M. Koshino, Anomalous Hall effect in 2H-phase MX₂ transition-metal dichalcogenide monolayers on ferromagnetic substrates ($M = \text{Mo, W}$ and $X = \text{S, Se, Te}$), *Phys. Rev. B* **96**, 085411 (2017).
- [26] H. Matsuoka, T. Habe, Y. Iwasa, M. Koshino, and M. Nakano, Spontaneous spin-valley polarization in NbSe₂ at a van der Waals interface, *Nat. Commun.* **13**, 5129 (2022).
- [27] S.-Y. Yang, Y. Wang, B. R. Ortiz, D. Liu, J. Gayles, E. Derunova, R. Gonzalez-Hernandez, L. Smejkal, Y. Chen, S. S. Parkin, S. D. Wilson, E. S. Toberer, T. McQueen, and M. N. Ali, Giant, unconventional anomalous Hall effect in the metallic frustrated magnet candidate, KV₃Sb₅, *Sci. Adv.* **6**, eabb6003 (2020).
- [28] K. Kang, T. Li, E. Sohn, J. Shan, and K. F. Mak, Nonlinear anomalous Hall effect in few-layer WTe₂, *Nat. Mater.* **18**, 324 (2019).
- [29] G. Kresse and J. Furthmüller, Efficient iterative schemes for *ab initio* total-energy calculations using a plane-wave basis set, *Phys. Rev. B* **54**, 11169 (1996).
- [30] G. Kresse and J. Furthmüller, Efficiency of *ab-initio* total energy calculations for metals and semiconductors using a plane-wave basis set, *Comput. Mater. Sci.* **6**, 15 (1996).

- [31] P. E. Blochl, Projector augmented-wave method, *Phys. Rev. B* **50**, 17953 (1994).
- [32] G. Kresse and D. Joubert, From ultrasoft pseudopotentials to the projector augmented-wave method, *Phys. Rev. B* **59**, 1758 (1999).
- [33] J. P. Perdew, K. Burke, and M. Ernzerhof, Generalized gradient approximation made simple, *Phys. Rev. Lett.* **77**, 3865 (1996).
- [34] H. J. Monkhorst and J. D. Pack, Special points for Brillouin-zone integrations, *Phys. Rev. B* **13**, 5188 (1976).
- [35] S. Grimme, Semiempirical GGA-type density functional constructed with a long-range dispersion correction, *J. Comput. Chem.* **27**, 1787 (2006).
- [36] S. L. Dudarev, G. A. Botton, S. Y. Savrasov, C. J. Humphreys, and A. P. Sutton, Electron-energy-loss spectra and the structural stability of nickel oxide: An LSDA+U study, *Phys. Rev. B* **57**, 1505 (1998).
- [37] H. Kumar, N. C. Frey, L. Dong, B. Anasori, Y. Gogotsi, and V. B. Shenoy, Tunable magnetism and transport properties in nitride MXenes, *ACS Nano* **11**, 7648 (2017).
- [38] X. Gonze and J.-P. Vigneron, Density-functional approach to nonlinear-response coefficients of solids, *Phys. Rev. B* **39**, 13120 (1989).
- [39] A. Togo and I. Tanaka, First principles phonon calculations in materials science, *Scr. Mater.* **108**, 1 (2015).
- [40] N. Marzari, A. A. Mostofi, J. R. Yates, I. Souza, and D. Vanderbilt, Maximally localized Wannier functions: Theory and applications, *Rev. Mod. Phys.* **84**, 1419 (2012).
- [41] Q. Wu, S. Zhang, H.-F. Song, M. Troyer, and A. A. Soluyanov, WANNIERTOOLS: An open-source software package for novel topological materials, *Comput. Phys. Commun.* **224**, 405 (2018).
- [42] D. J. Thouless, M. Kohmoto, M. P. Nightingale, and M. den Nijs, Quantized Hall conductance in a two-dimensional periodic potential, *Phys. Rev. Lett.* **49**, 405 (1982).
- [43] X. Wang, J. R. Yates, I. Souza, and D. Vanderbilt, *Ab initio* calculation of the anomalous Hall conductivity by Wannier interpolation, *Phys. Rev. B* **74**, 195118 (2006).
- [44] D. Xiao, M.-C. Chang, and Q. Niu, Berry phase effects on electronic properties, *Rev. Mod. Phys.* **82**, 1959 (2010).
- [45] F. A. Rasmussen and K. S. Thygesen, Computational 2D materials database: Electronic structure of transition-metal dichalcogenides and oxides, *J. Phys. Chem. C* **119**, 13169 (2015).
- [46] H. Y. Lv, W. J. Lu, D. F. Shao, Y. P. Liu, and Y. Sun, Strain-controlled switch between ferromagnetism and antiferromagnetism in 1T-CrX₂ (X = Se, Te) monolayers, *Phys. Rev. B* **92**, 214419 (2015).
- [47] H. L. Zhuang, M. D. Johannes, M. N. Blonsky, and R. G. Hennig, Computational prediction and characterization of single-layer CrS₂, *Appl. Phys. Lett.* **104**, 022116 (2014).
- [48] M. R. Habib, S. Wang, W. Wang, H. Xiao, S. M. Obaidulla, A. Gayen, Y. Khan, H. Chen, and M. Xu, Electronic properties of polymorphic two-dimensional layered chromium disulphide, *Nanoscale* **11**, 20123 (2019).
- [49] C. Ataca, H. Sahin, and S. Ciraci, Stable, single-layer MX₂ transition-metal oxides and dichalcogenides in a honeycomb-like structure, *J. Phys. Chem. C* **116**, 8983 (2012).
- [50] X.-H. Tian and J.-M. Zhang, The electronic, magnetic and optical properties of single-layer CrS₂ with vacancy defects, *J. Magn. Magn. Mater.* **487**, 165300 (2019).
- [51] M. Pandey, A. Vojvodic, K. S. Thygesen, and K. W. Jacobsen, Two-dimensional metal dichalcogenides and oxides for hydrogen evolution: A computational screening approach, *J. Phys. Chem. Lett.* **6**, 1577 (2015).
- [52] C. Lei, Y. Ma, T. Zhang, X. Xu, B. Huang, and Y. Dai, Valley polarization in monolayer CrX₂ (X = S, Se) with magnetically doping and proximity coupling, *New J. Phys.* **22**, 033002 (2020).
- [53] See Supplemental Material <http://link.aps.org/supplemental/10.1103/PhysRevB.110.125406> for geometry and stability of monolayers, comparison between 2H and 1T phases of CrS₂ monolayer, electronic properties of monolayers, stacking orders of CrS₂/CrBr₃ heterostructure, interface binding energy and stability of vdW heterostructure, electronic properties of CrS₂/CrBr₃ heterostructure, magnetic proximity effect with on-site interaction, and the Wannier tight-binding model. The Supplemental Material also contains Refs. [54–59].
- [54] W. Chen, Z. Sun, Z. Wang, L. Gu, X. Xu, S. Wu, and C. Gao, Direct observation of van der Waals stacking-dependent interlayer magnetism, *Science* **366**, 983 (2019).
- [55] N. Maity, P. Srivastava, H. Mishra, R. Shinde, and A. K. Singh, Anisotropic interlayer exciton in GeSe/SnS van der Waals heterostructure, *J. Phys. Chem. Lett.* **12**, 1765 (2021).
- [56] J. Wang, Z. Guan, J. Huang, Q. Li, and J. Yang, Enhanced photocatalytic mechanism for the hybrid g-C₃N₄/MoS₂ nanocomposite, *J. Mater. Chem. A* **2**, 7960 (2014).
- [57] Y. Choi, J. W. Villanova, and K. Park, Zeeman-splitting-induced topological nodal structure and anomalous Hall conductivity in ZrTe₅, *Phys. Rev. B* **101**, 035105 (2020).
- [58] J. W. Villanova and K. Park, Magnetic field induced Weyl semimetal from Wannier-function-based tight-binding model, *Phys. Rev. B* **98**, 075123 (2018).
- [59] C. Si, Z. Lin, J. Zhou, and Z. Sun, Controllable Schottky barrier in GaSe/graphene heterostructure: The role of interface dipole, *2D Mater.* **4**, 015027 (2016).
- [60] W. B. Zhang, Q. Qu, P. Zhu, and C. H. Lam, Robust intrinsic ferromagnetism and half semiconductivity in stable two-dimensional single-layer chromium trihalides, *J. Mater. Chem. C* **3**, 12457 (2015).
- [61] C. Bacaksiz, D. Sabani, R. M. Menezes, and M. V. Milosevic, Distinctive magnetic properties of CrI₃ and CrBr₃ monolayers caused by spin-orbit coupling, *Phys. Rev. B* **103**, 125418 (2021).
- [62] I. Žutić, J. Fabian, and S. D. Sarma, Spintronics: Fundamentals and applications, *Rev. Mod. Phys.* **76**, 323 (2004).
- [63] J. Zhao, X. Jin, H. Zeng, C. Yao, and G. Yan, Spin-valley coupling and valley splitting in the MoSi₂N₄/CrCl₃ van der Waals heterostructure, *App. Phys. Lett.* **119**, 213101 (2021).
- [64] B. Zhu, H. Zeng, J. Dai, Z. Gong, and X. Cui, Anomalously robust valley polarization and valley coherence in bilayer WS₂, *Proc. Natl. Acad. Sci. USA* **111**, 11606 (2014).
- [65] S. Guddala *et al.*, All-optical nonreciprocity due to valley polarization pumping in transition metal dichalcogenides, *Nat. Commun.* **12**, 3746 (2021).
- [66] G. Yang, J. Li, H. Ma, Y. Yang, C. Li, X. Mao, and F. Yin, Induced valley splitting in monolayer MoS₂ by an antiferromagnetic insulating CoO(111) substrate, *Phys. Rev. B* **98**, 235419 (2018).

- [67] L. Xu, M. Yang, L. Shen, J. Zhou, T. Zhu, and Y. P. Feng, Large valley splitting in monolayer WS_2 by proximity coupling to an insulating antiferromagnetic substrate, *Phys. Rev. B* **97**, 041405(R) (2018).
- [68] J. H. Dil, Finding spin hedgehogs in chiral crystals, *Physics* **13**, 45 (2020).
- [69] T. Zhang, X. Xu, B. Huang, Y. Dai, and Y. Ma, 2D spontaneous valley polarization from inversion symmetric single-layer lattices, *npj Comput. Mater.* **8**, 64 (2022).
- [70] D. Xiao, W. Yao, and Q. Niu, Valley-contrasting physics in graphene: Magnetic moment and topological transport, *Phys. Rev. Lett.* **99**, 236809 (2007).
- [71] Y. Ren, J. Zeng, X. Deng, F. Yang, H. Pan, and Z. Qiao, Quantum anomalous Hall effect in atomic crystal layers from in-plane magnetization, *Phys. Rev. B* **94**, 085411 (2016).
- [72] M. C. Chang and Q. Niu, Berry phase, hyperorbits, and the Hofstadter spectrum: Semiclassical dynamics in magnetic Bloch bands, *Phys. Rev. B* **53**, 7010 (1996).